

Elsevier required licence: © <2019>. This manuscript version is made available under the CC-BY-NC-ND 4.0 license
<http://creativecommons.org/licenses/by-nc-nd/4.0/>
The definitive publisher version is available online at
[<https://www.sciencedirect.com/science/article/abs/pii/S0946672X18304243?via%3Dihub>]

1 **LA-ICP-MS/MS improves limits of detection**
2 **in elemental bioimaging of gadolinium**
3 **deposition originating from MRI contrast**
4 **agents in skin and brain tissues**

5
6 David Clases^{1,2}, Stefanie Fingerhut¹, Astrid Jeibmann³, Michael Sperling^{1,4},
7 Philip Doble², Uwe Karst¹

8
9 ¹University of Münster, Institute of Inorganic and Analytical Chemistry,
10 Corrensstr. 30, 48149 Münster, Germany

11 ²Elemental Bioimaging Facility, University of Technology Sydney, Broadway,
12 New South Wales, Australia

13 ³University Hospital Münster, Institute of Neuropathology, Pottkamp 2,
14 48149 Münster, Germany

15 ⁴European Virtual Institute for Speciation Analysis (EVISA), Mendelstraße 11,
16 48149 Münster, Germany

17
18
19 **Keywords:** Gadolinium retention, NSF, LA-ICP-MS, ICP-MS/MS, Quantitative
20 bioimaging

21 **Category:** Research paper
22
23

24 **Abstract**

25 A novel analytical method to detect the retention of gadolinium from contrast
26 agents for magnetic resonance imaging (MRI) in tissue samples of patients is
27 presented. It is based on laser ablation - inductively coupled plasma - triple
28 quadrupole - mass spectrometry (LA-ICP-MS/MS). Both Gd and P were
29 monitored with a mass shift of +16, corresponding to mono-oxygenated species,
30 as well as Zn, Ca, and Fe on-mass. This method resulted in a significantly
31 reduced background and improved limits of detection not only for phosphorus,
32 but also for gadolinium. These improvements were essential to perform elemental
33 bioimaging with improved resolution of 5 μm x 5 μm , allowing the detection of
34 small Gd deposits in fibrotic skin and brain tumour tissue with diameters of
35 approximately 50 μm . Detailed analyses of these regions revealed that most Gd
36 was accompanied with P and Ca, indicating co-precipitation.

37

38

39

40 **Introduction**

41 The deposition of Gd originating from Gd-based contrast agents (GBCAs) in
42 biological tissue has caused major concerns in the past decade. Grobner *et al.*
43 first identified that Gd may be retained inside the body and may lead to a
44 potentially fatal disease known as nephrogenic systemic fibrosis (NSF) [1]. NSF
45 was first observed in patients with impaired renal function [2,3]. It took a further
46 six years for the correlation of the development of NSF with the administration of
47 GBCAs for magnetic resonance imaging (MRI) examinations conducted several
48 years before [4]. Pathologies such as diffuse ulcerative calcific atherosclerosis,
49 patchy myocardial necrosis, fibrosis and necrotic skin were also identified in
50 patients with MRI history without renal dysfunction [5]. Kasahara *et al.* reported
51 that Gd can be found in the dentate nucleus of MRI patients with a history of brain
52 irradiation [6]. Xia *et al.* also identified Gd deposits in brain tumour samples
53 obtained from five MRI patients without renal dysfunction by energy dispersive X-
54 ray spectroscopy (SEM/EDS), and demonstrated that the deposits also contained
55 Ca and P [7]. Ever since a FDA safety announcement in 2015 [8], the retention
56 of Gd has attracted more concerns and triggered further investigations which
57 were reviewed recently [9].

58 The development of NSF appears to be highly dependent on the type of the
59 GBCA administered as different forms have disparate retention of Gd in the brain
60 and other organs. Nevertheless, Gd retention in NSF and brain tissues has been
61 reported for all categories (ionic/non-ionic, linear/macrocyclic) of GBCAs. Non-
62 ionic, linear GBCAs have been identified as the most problematic [10–13]. Birka
63 *et al.* were able to show the presence of intact GBCAs in NSF skin biopsies of a
64 patient by hydrophilic interaction liquid chromatography (HILIC) coupled to ICP-
65 MS, as well as confirm the deposition and accumulation of Gd with Ca and P of
66 in NSF tissues by laser ablation-inductively coupled plasma-mass spectrometry
67 (LA-ICP-MS) [14]. These results were subsequently confirmed by Roberts *et*
68 *al.* [15].

69 Recently, Fingerhut et al. demonstrated the retention of Gd in specific brain
70 regions of humans treated with GBCAs and located Gd in distinct cell types within
71 these regions [16,17]. The pathogenesis of NSF as well as the mechanism of
72 retention of Gd in specific brain regions such as the dentate nucleus still is largely
73 unknown. Although GBCAs are considered to be thermodynamically stable and
74 kinetically inert, it is hypothesised that Gd is released and precipitates, possibly
75 together with calcium as (mixed) phosphate. Transmetallation reactions are
76 suspected to play a crucial role for the release of Gd [5,18], as well as metabolism
77 and elimination of GBCAs, which is compromised in patients with renal
78 dysfunction [19]. The formation of small deposits of Gd and coprecipitation with
79 Ca and P within various organs has been observed with imaging techniques such
80 as element specific transmission electron microscopy (TEM), scanning electron
81 microscopy/energy dispersive X-ray spectroscopy (SEM/EDX), secondary ion
82 mass spectrometry (SIMS), synchrotron X-ray fluorescence (SXRF) and
83 extended X-ray absorption fine structure (EXAFS) spectroscopy [7,19–27].
84 However, the relationship of these deposits and the pathogenesis of NSF has not
85 been fully explored. One hypothesis is that circulating fibrocytes respond to the
86 deposits to initiate fibrosis.[28]

87 Accordingly, the investigation of the mechanism of NSF progression in relation to
88 Gd deposits with diameters of approximately 50 μm requires a method that is
89 capable of quantitative imaging with high spatial resolution and low limits of
90 detection. Triple quadrupole technology for ICP-MS enhances the analysis of
91 many elements by performing tandem mass spectrometry and was first
92 hyphenated to a LA system in 2016 for elemental bioimaging [29]. Tandem mass
93 spectrometry for ICP-MS has enhanced detection capabilities for many elements
94 to improve detection limits and remove potential interferences. One approach to
95 avoid spectral interferences is by shifting the analytes' mass with favoured
96 chemical reactions in the collision/reaction cell by adding a dedicated reaction
97 gas. The selection of the reaction gas, the reaction conditions and the impact on
98 the analysis must be evaluated carefully. Bolea-Fernandez et al. and Balcaen et

99 al reviewed the theoretical background and recent applications, methods, theory
100 and instrumentation [30,31].

101 In this work, we present a new method for the investigation of Gd deposition in a
102 NSF skin sample as well as in a cancerous brain sample of a MRT patient by LA-
103 tandem ICP-MS. The limits of detection (LOD) for trace elements believed to play
104 a key role in NSF, such as Gd, P, Ca, Fe and Zn, were compared against single
105 quadrupole LA-ICP-MS to demonstrate the advantages of the LA-ICP-MS/MS
106 method.

107 **1.1 Experimental**

108 **1.1.1 Sample Preparation**

109 For elemental bioimaging (EBI), NSF samples were obtained from the “*Johannes*
110 *Wesling Klinikum*” (hospital) in Minden in April 2013 and originate from a 25-year-
111 old female patient. A biopsy of an affected skin area was taken and immediately
112 frozen to -20 °C. The patient showed typical NSF symptoms including swollen
113 and sclerotic skin. The clinical history included a kidney transplantation and on-
114 going impaired renal function requiring regular dialysis. The patient underwent
115 MRI examinations with the linear GBCA gadopentetate (Gd-DTPA, Bayer Vital
116 (Leverkusen, Germany)) in 2002, and with the macrocyclic GBCA gadoteridol
117 (Gd-HP-DO3A, Bracco Imaging, 0.5 M (Konstanz, Germany)) in 2005. The first
118 symptoms appeared two years prior to the skin biopsy. For analysis, the skin
119 sample was cut axially to 20 µm thickness using a cryotome (CryoStat™ NX70,
120 Thermo Fisher Scientific) at -30 °C and placed onto glass slides. For a
121 histological grading, a sequential slide was stained with hematoxylin and eosin
122 (H&E) to visualise tissue structures.

123 Brain tumour samples were obtained from the archives of the Institute of
124 Neuropathology, University Hospital Münster and originated from a female 77
125 years old patient who was suffering from a glioblastoma, IDH wild type (grade IV

126 WHO). She underwent an MRI examination with 20 mL of Gd-HP-DO3A.
127 Samples were collected eleven days after the MRI examination during a biopsy
128 and immediately frozen to -20 °C, cut to a thickness of 20 µm and mounted onto
129 glass slides.

130 For both patients, it should be noted that it cannot be excluded that they received
131 Gd-based contrast agents prior to the treatment period which is documented
132 above. Therefore, the Gd deposition detected in this work cannot be
133 unambiguously traced back to the contrast agents, which are known to have been
134 delivered.

135 **1.1.2 Calibration strategy**

136 Quantification of Gd and the determination of LODs of the elements of interest
137 were performed by in-house prepared matrix-matched standards consisting of
138 homogenised lamb brain spiked with respective elements and mounted in thin
139 tissue sections with a thickness of 20 µm on glass slides. A detailed procedure
140 for the fabrication, storage, quality control as well as the data analysis was
141 already reported earlier by Hare *et al.* [32]. The matrix-matched standards were
142 counter-quantified after digestion with 1 mL 30-32% H₂O₂ and 4 mL 70% HNO₃
143 (Seastar Baseline, Choice Analytical, Galveston, USA) using conventional liquid
144 sample introduction with a 7500cx ICP-MS system (Agilent Technologies,
145 Mulgrave, Victoria, Australia), shown in Table 1. The accuracy of the approach
146 was validated using a BCR185R bovine liver reference standard.

147 Table 1. Concentration levels of P, Ca, Fe, Zn and Gd present in the (matrix-matched)
148 standards used for the generation of calibration curves and the subsequent
149 determination of LODs. *In case of P, diluted standard solutions instead of spiked matrix
150 samples were used for calibration.

| Level | P* [ng/g] | Ca [µg/g] | Fe [µg/g] | Zn [µg/g] | Gd [µg/g] |
|-------|-----------|-----------|-----------|-----------|-----------|
| 1 | 0 | 37.7 | 15.3 | 11.3 | 0.00 |
| 2 | 0.001 | 43.0 | 16.5 | 11.4 | 0.21 |

| | | | | | |
|---|------|------|------|------|------|
| 3 | 0.01 | 48.7 | 19.0 | 14.9 | 2.21 |
| 4 | 1 | 64.1 | 37.5 | 24.0 | 10.6 |
| 5 | 10 | 86.4 | 59.8 | 36.1 | 21.1 |

151

152 **1.1.3 Instrumentation and Tune Development**

153 For EBI, elements of interest were analysed with individual integration times on
154 a 8800 series ICP-MS/MS system (Agilent Technologies, Mulgrave, Victoria,
155 Australia) coupled to a New Wave Research NWR193 laser ablation unit
156 (Kennelec Scientific, Mitcham, Victoria, Australia). ($^{31}\text{P}/^{31}\text{P}^{16}\text{O}$: 50 ms, ^{44}Ca :
157 40 ms, ^{57}Fe : 35 ms, ^{64}Zn : 35 ms, $^{158}\text{Gd}/^{158}\text{Gd}^{16}\text{O}$, 47 ms). The single quadrupole
158 (SQ) tune was developed according to Lear *et al.*[33] The laser scan speed and
159 the spot size of the ArF excimer laser emitting nanosecond laser pulses at
160 193 nm were adapted to generate squared pixels. For preliminary scans and
161 comparison of LA-ICP-MS/MS against the LA-ICP-SQ-MS tunes, 50 μm laser
162 beam spot size and 200 $\mu\text{m}/\text{s}$ scan speed were chosen. For the high-resolution
163 images, the parameters were adjusted to 5 μm and 20 $\mu\text{m}/\text{s}$, respectively. The
164 sensitivity of the ICP-MS system was monitored on a daily basis and optimised
165 with a tune solution containing ^7Li , ^{89}Y and ^{205}Tl . A low oxide formation was
166 guaranteed by monitoring the ThO/Th ratio (<0.3 %) and the P/A factor was
167 adjusted before each measurement. For the MS/MS tune development, the
168 ICP-MS/MS system was equipped with a MicroMist concentric nebuliser
169 (Elemental Scientific, Omaha, NE, USA) and a Scott-type double-pass spray
170 chamber (Glass Expansion, West Melbourne, Victoria, Australia). Using this
171 liquid sample introduction system arrangement, plasma independent parameters
172 were optimised to achieve lower LODs. Finally, dry plasma conditions were
173 adapted for the operation of LA-ICP-MS. The initial tuning was performed by
174 ablation of a NIST 612 “Trace Element in Glass” certified reference material
175 (CRM), whereas the fine tuning was performed by monitoring the m/z of interest
176 during the ablation of matrix-matched standards. The optimised tune parameters
177 were: cell entrance, -75 V; OctP RF, 180 V; OctP bias, -5 V; deflect, 5 V; energy

178 discrimination, -8 V; O₂ cell gas flow, 0.32 mL/min; waiting time offset, 8 ms. To
179 avoid long settling times caused by multiple filling and evacuation of the
180 collision/reaction cell, all elements of interest were analysed with oxygen present
181 as reaction gas. However, only P and Gd were monitored with a + 16 amu mass
182 shift. In SQ mode, the first quadrupole was used as a band-pass filter and the
183 ICP-MS/MS system provided the best figures of merit for all analytes when
184 operating the collision/reaction cell with H₂ gas flow of 3 mL/min [33]. To compare
185 the figures of merit of both tunes, LODs were calculated based on the 3σ criterion
186 by ablating line scans on matrix-matched tissue sections with a laser spot size of
187 50 μm and a scan speed of 200 μm/s. The standard deviation was derived from
188 the shutter blank and the respective sensitivities from five-point calibration
189 curves. In the case of P, the natural background and the variations in matrix-
190 matched tissue derived from living organisms were too high for the estimation of
191 the benefits of ICP-MS/MS over ICP-SQ-MS. Therefore, generation of a
192 calibration curve for the determination of the LODs was conducted with diluted
193 standard solutions on a liquid sample introduction system as described previously
194 to demonstrate the advantages of the MS/MS tune. Quantification of high
195 resolution data obtained using a laser beam spot size of 5 μm was solely
196 conducted for Gd. A calibration curve was generated considering the standard
197 deviations of each calibration point. The deviations were weighted according to
198 equation 1. The deviation of 0 cps at a Gd concentration of 0 μg/g was weighted
199 with 1.

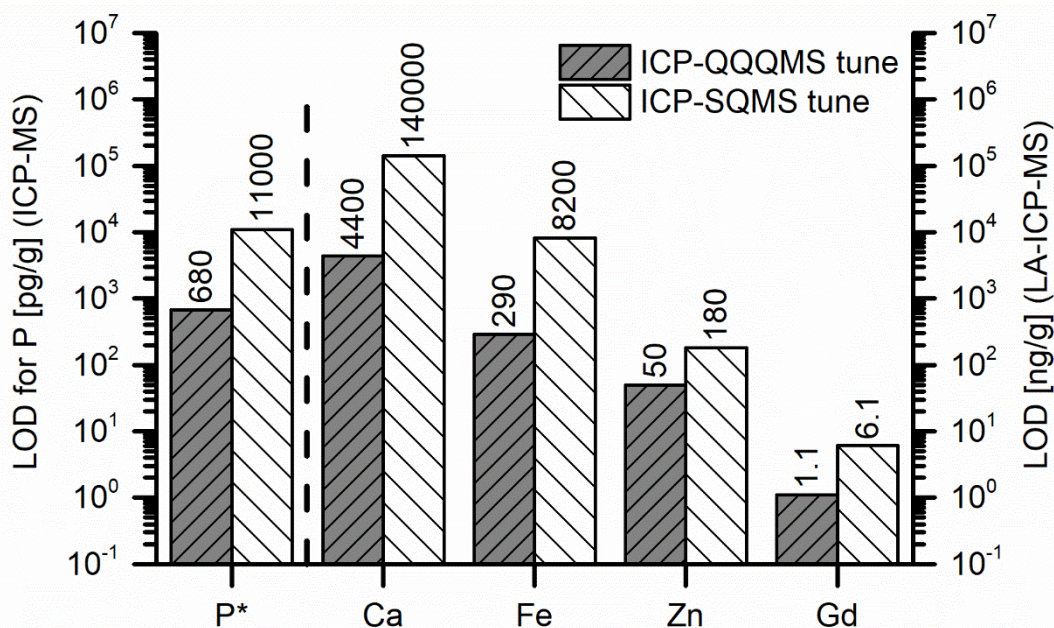
$$200 \quad \omega = \frac{1}{\sigma^2} \quad (1)$$

201 Where, ω is the weighting factor and σ is the standard deviation. The ICP-MS/MS
202 system was operated with MassHunter software (Agilent Technologies). The LA
203 unit was operated with ActiveView software (Electro Scientific Industries,
204 Portland, Oregon, USA). The analytical figures of merit were processed using
205 Origin software version 9 (OriginLab Corporation, Northampton, MA, USA).
206 Element images were generated using MassImager 3.17 software, an in-house
207 developed program for image visualisation.

208 **1.2 Results and Discussion**

209 **1.2.1 Tune Development for EBI**

210 On-mass or mass-shift MS/MS detection requires consideration of the reaction
211 enthalpies. Both P and Gd have negative reaction enthalpies with O₂ and were
212 amenable for mass-shift monitoring at +16 amu. The remaining target elements
213 Ca, Fe and Zn were monitored on-mass. Oxygen acted here as both reaction and
214 collision gas. For the oxophilic elements P and Gd, mass shifting and tandem
215 mass spectrometry resulted in a reduced background and therefore overall
216 improved signal to noise ratios. The elements Ca, Zn and Fe showed improved
217 figures of merit when analysed on-mass due to the collisional elimination of
218 polyatomic interferences. The benefits of such detection modes for the elements
219 were demonstrated via comparison of LODs against a standard ICP-SQ-MS
220 method. The LODs were estimated by construction of calibration curves by LA
221 line scans (50 μm spot size) of the matrix matched standards and application of
222 the 3σ criterion or by estimation of the minimal detectable concentration (Figure
223 1). In case of P, the determination of the LODs was performed via liquid standards
224 as the matrix matched tissue standards had high backgrounds and variable
225 content.



226

227 Figure 1. Comparison of LODs obtained by (LA-)ICP-MS/MS and (LA-)ICP-SQ-MS. *In
 228 case of P, LODs were determined using a calibration curve obtained from diluted
 229 standards introduced via a liquid sample introduction system whereas the LODs of Gd,
 230 Fe, Ca and Zn originate from the dry plasma MS/MS tune performed in line-by-line scans
 231 on matrix-matched standards by LA-ICP-MS/MS.

232 Due to highly abundant isobaric polyatomic interferences in the low mass range,
 233 the MS/MS tune for P resulted in a crucial improvement of 16.2-fold lower LODs.
 234 In case of Gd, the MS/MS tune eliminated the background to 0 cps, precluding
 235 the calculation of the LOD with the 3σ criterion. Instead, we used the lowest
 236 concentration (1.1 ng/g) that provided the least measurable signal (21 counts/s).
 237 This value was a 5.5-fold improvement compared against the ICP-SQ mode. For
 238 Fe, Ca and Zn, the ICP-MS/MS improvement factors were 28.3, 31.8, and 3.6,
 239 respectively.

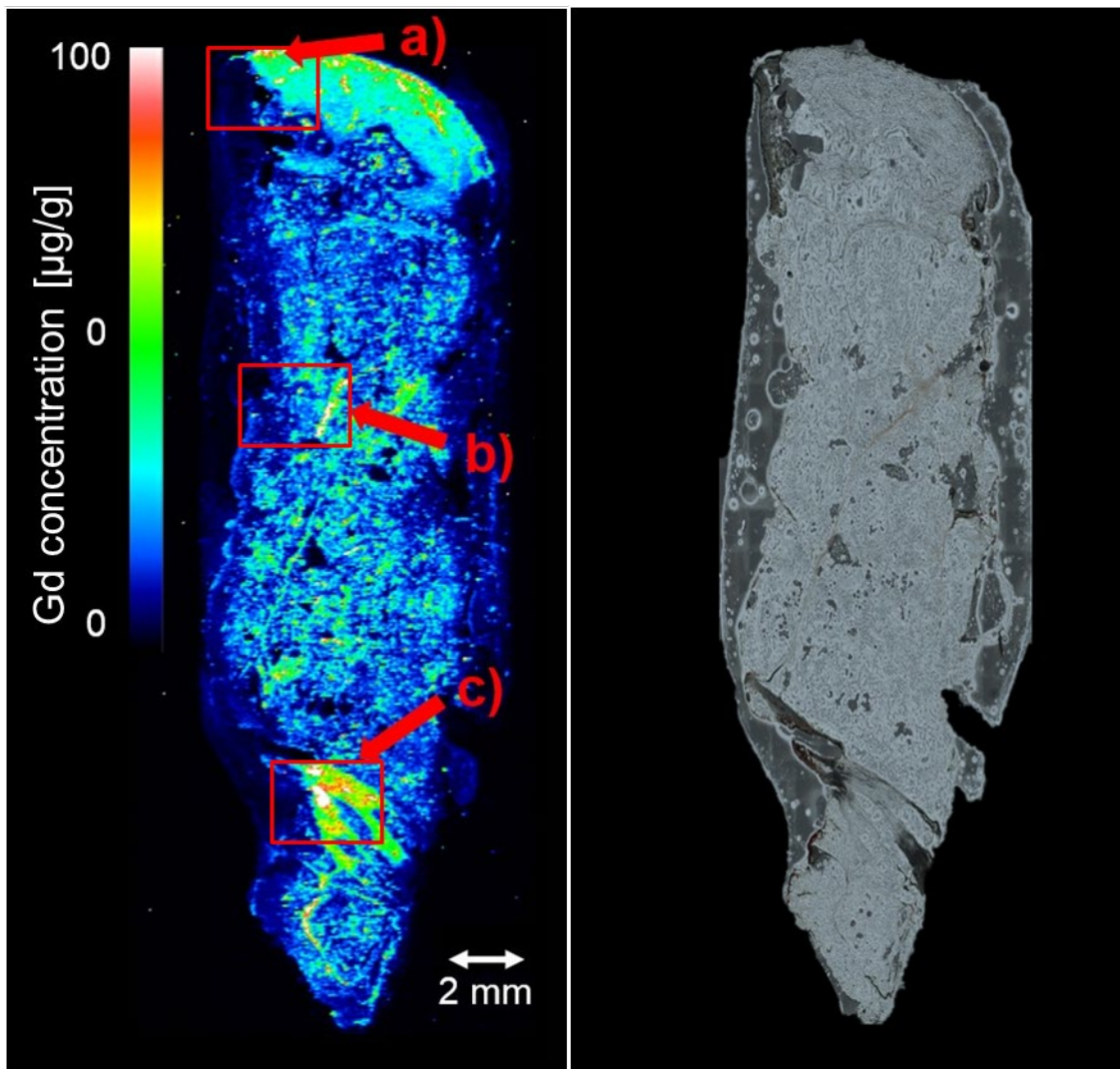
240 These improved LODs of the ICP-MS/MS were essential to successfully image,
 241 characterise and quantify the Gd deposits at higher resolutions of 5 μm . The
 242 LODs for Gd obtained by the 5 μm LA-ICP-MS/MS tune was 48 ng/g.

243 **1.2.2 NSF skin samples**

244 The large dimensions of the sample (approximately 3 cm x 0.8 cm) spanning
245 various anatomical structures required a low resolution preliminary scan (pixel
246 dimensions: 50 μm x 50 μm) to disclose regions of interest with dense
247 distributions of Gd deposits. Figure 2 shows the quantitative distribution of Gd in
248 the NSF skin sample and the corresponding microscopic image.

249 Although there were hot spots of Gd deposits located throughout the sample
250 (Figure 2), there were three areas of obvious accumulation, labelled (a), (b) and
251 (c). Region of interest (a) had the most dense distribution of pixels with
252 concentrations calculated via extrapolation to exceed 100 $\mu\text{g/g}$. Regions (b) and
253 (c) consisted of a blood vessel and connective tissue, respectively, and had
254 concentrations also exceeding 100 $\mu\text{g/g}$. Area (a) was targeted for further
255 investigation with a higher resolution of 5 μm .

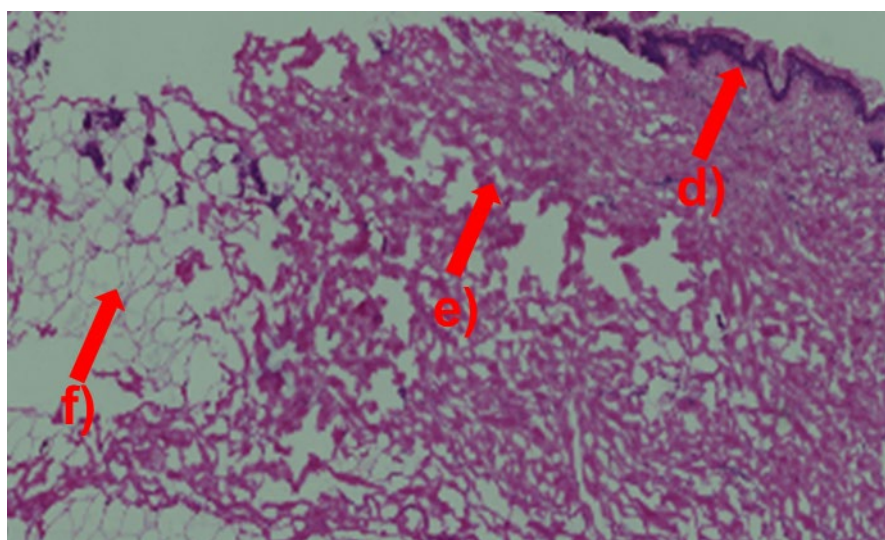
256



257

258 Figure 2. Comparison of the elemental Gd distribution and the corresponding
 259 microscopic image. **Left:** Quantitative Gd distribution obtained by LA-ICP-MS/MS with a
 260 spatial resolution of 50 μm . Three regions of interest are designated. Region (a) showed
 261 a distribution of hot spots in the sub cutis with concentrations exceeding 100 $\mu\text{g/g}$, (b)
 262 contains a blood vessel and (c) exhibits connective tissue in the deeper skin. **Right:**
 263 Corresponding microscopic image.

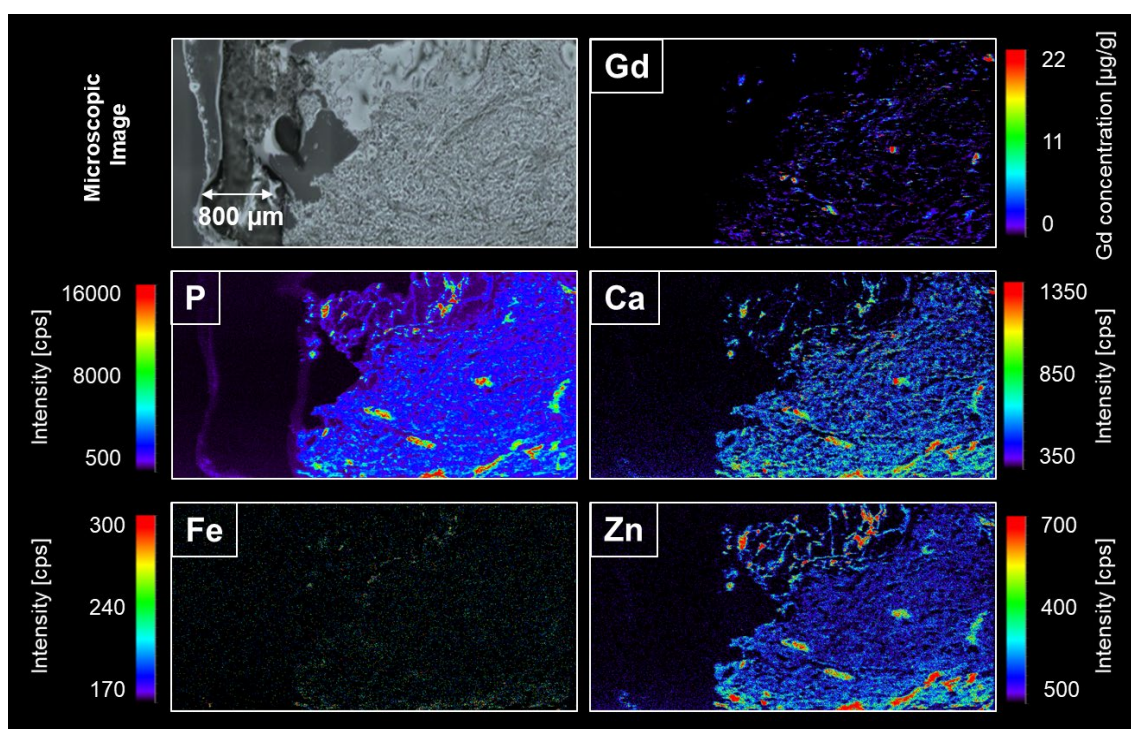
264 Various layers of the skin within the region of interest were identified by a
 265 haematoxylin and eosin (H&E) stain of a consecutive section, which is shown in
 266 Figure 3. The epidermis is visible at (d), and fibrotic tissue at location (e) can be
 267 seen intermingled with fatty tissue areas (f). These histological findings are
 268 similar to those as described by Schäd *et al.*[21]



269

270 Figure 3. H&E stained NSF skin of a consecutive tissue section (corresponding to region
271 of interest (a), shown in Figure 2). Different anatomical areas can be seen: epidermis
272 (d), fatty tissue (f) and fibrotic tissue (e).

273 A high-resolution ($5\ \mu\text{m} \times 5\ \mu\text{m}$) LA-ICP-MS image of Gd, P, Ca, Fe and Zn, and
274 a light photomicrograph of area (a) are shown in Figure 4. The improved
275 resolution revealed hotspots of all target elements within small deposits of
276 approximately $50\ \mu\text{m}$ in the fibrotic tissue. The elemental distribution of Gd, P, Ca
277 and Zn correlated in location and shape clearly demonstrating the abundance of
278 insoluble phosphate species. Correlations with Fe were not observed. These
279 observations were consistent with other investigations by SIMS [22], SXRF and
280 EXAFS [20]. Smaller deposits were reported by Thakral *et al.* using TEM [19].

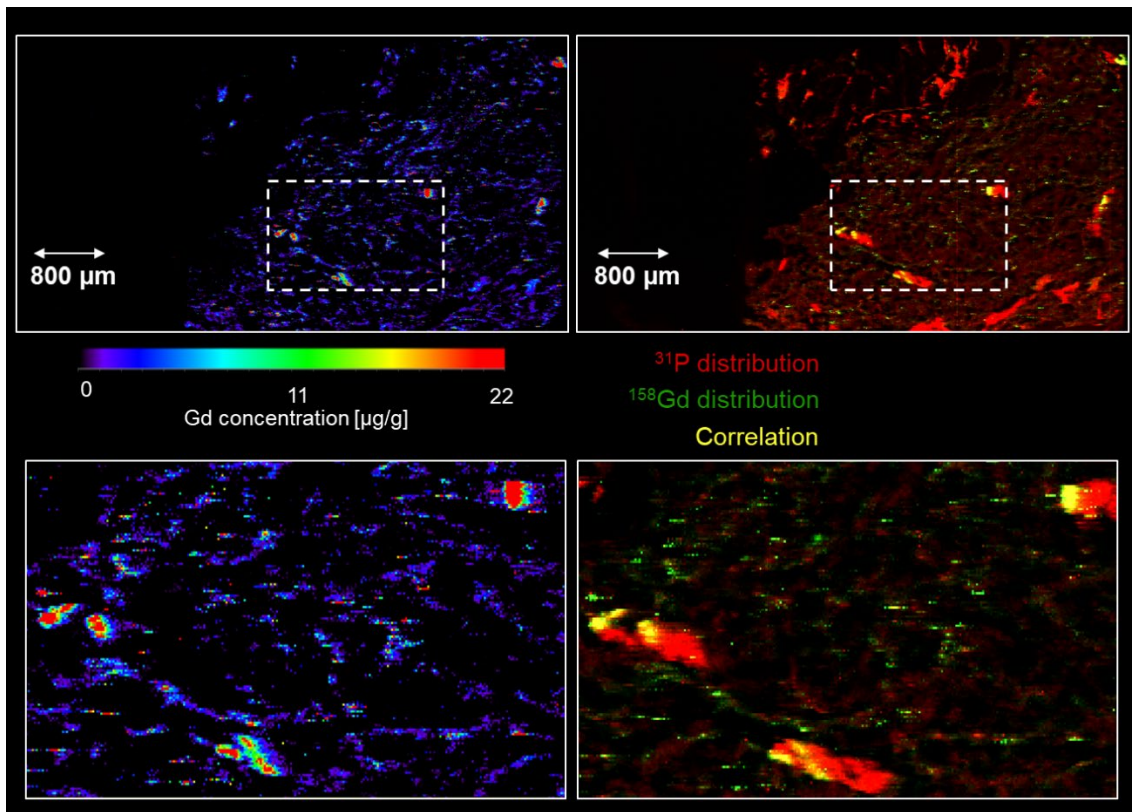


281

282 Figure 4. A light microscopic image of NSF skin tissue (area a, Figure 3) and the
 283 elemental distributions of Gd, P, Ca and Zn. Except for Fe, all elements show strong
 284 correlations.

285 Figure 5 presents a zoom view of area (a) to further visualise the composition of
 286 the deposits. Most of the Gd throughout the specimen was located within the
 287 deposits with the highest concentrations in the centre exceeding $100 \mu\text{g/g}$. An
 288 overlay of Gd (green) and P (red) clearly shows co-localisation within the
 289 deposits. Similar correlations were found in accumulations for Ca and Zn. The
 290 most likely explanation for this distribution is the co-precipitation of Gd with
 291 calcium and zinc phosphate, when the concentration of the circulating free Gd
 292 and phosphate ions exceeds the solubility limits of Gd-phosphate ($\text{pK}_{\text{SP}} = 25.39$).
 293 Only the core of the deposits is made of Gd whereas the shell seems to have an
 294 increasing fraction of P. This indicates that the Gd phosphate deposits may
 295 function as nucleation centre favouring the subsequent growth.

296



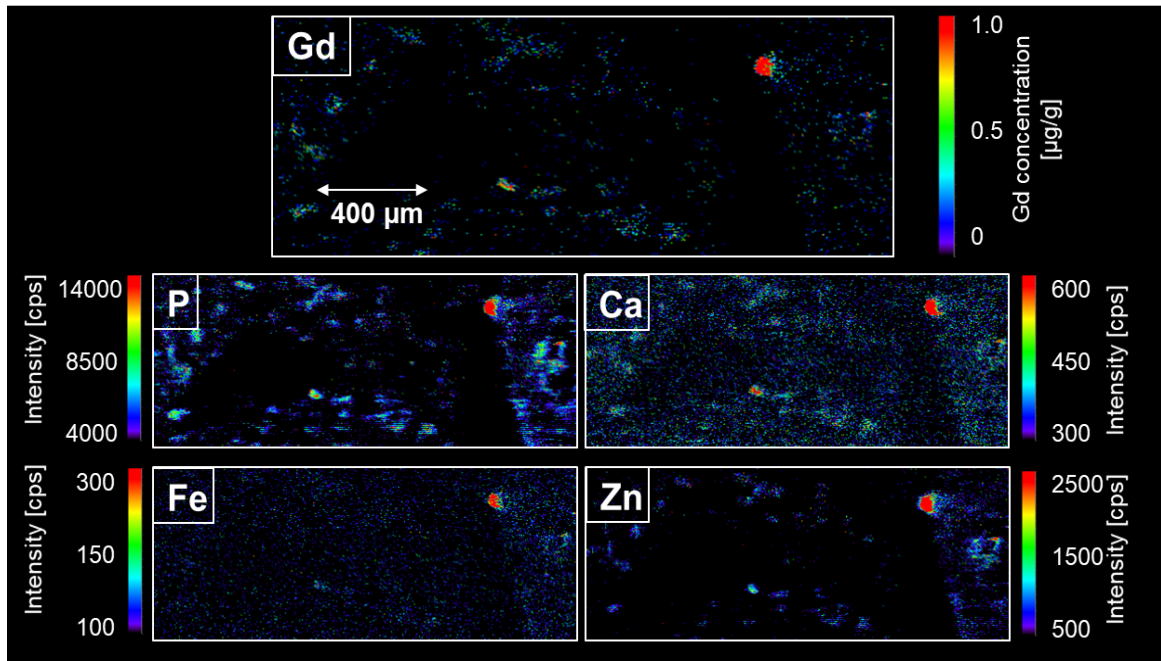
297

298 Figure 5. The Gd distribution in NSF skin tissue is shown and correlated to the distribution
 299 of P. **Left:** Zoomed views of the Gd distribution. The deposits contained most of the Gd
 300 found in the tissue sample. The centre of the deposits exhibited highest concentrations
 301 exceeding 100 µg/g. **Right:** Overlay of the ^{31}P distribution (red) and the Gd distribution
 302 (green). Correlations are shown in yellow, showing smaller areas of Gd within P areas.

303 **1.2.3 Brain Tumour Samples**

304 Gd deposition in the brain was investigated in a brain biopsy originating from a
 305 patient with a glioblastoma tumour (IDH wildtype, grade IV WHO). Progression of
 306 glioblastoma is known to increase the permeability of the blood brain barrier due
 307 to localised damage. It was suspected that this patient's tumour burden would
 308 lead to detectable deposits of Gd following administration of Gd-HP-DO3A.
 309 Figure 6 shows a 5 µm x 5 µm resolution image of the elemental distribution of
 310 the target elements in the brain tumour tissue. Like the deposits found in NSF
 311 skin tissue, the diameter was in the same range of approximately 50 µm x 50 µm
 312 or below. Correlations and co-localisation of Gd with P, Ca, Zn, as well as Fe
 313 were clearly evident. However, the Gd concentration in the tumour sample was a

314 factor of 25-100 times lower than in the skin biopsies. The concentration of Gd in
315 the deposits exceeded 1 $\mu\text{g/g}$ in some instances, whilst other accumulations had
316 lower concentrations between 0.2 $\mu\text{g/g}$ and 0.6 $\mu\text{g/g}$.
317



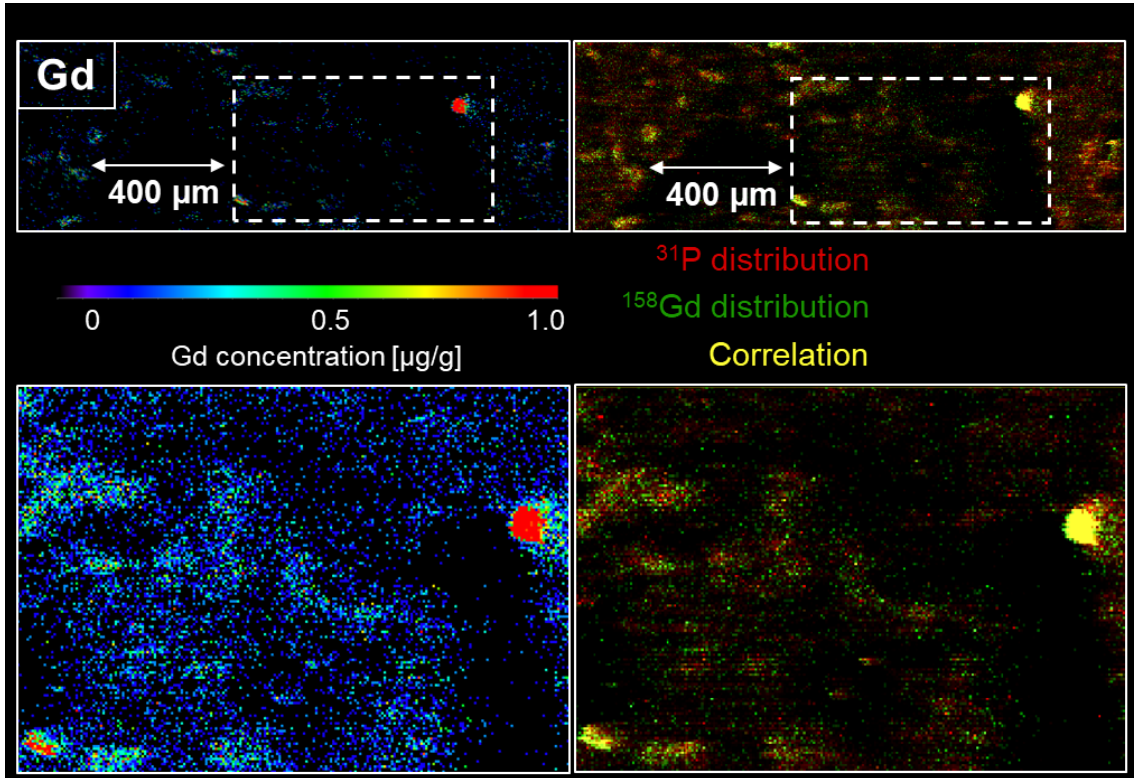
318

319 Figure 6. Elemental distribution of Gd, P, Ca, Zn and Fe in a brain tissue section. The
320 Gd distribution was calibrated using matrix-matched tissue standards.

321 These results are in agreement with findings from Xia *et al.*, who reported Gd
322 deposits smaller than 50 μm inside brain tumours using SEM/EDX, and similar
323 correlations with other elements.[7] Smaller deposits were reported in diseased
324 brain tissue by McDonald *et al.*[23]

325 Figure 7 presents a zoom view of the quantitative Gd distribution as well as an
326 overlay of the P distribution and the Gd distribution. Both distributions correlated
327 in terms of shape, dimensions and locations. These findings support preceding
328 studies that reported the formation of insoluble deposits containing P, Ca, Fe and
329 Zn. While such deposits in the brain seem to have very similar elemental
330 composition as those observed in the skin of NSF patients, the observed

331 concentration in the brain were significantly lower than determined in NSF skin
332 tissue.



333

334 Figure 7. Correlation of the Gd and P distribution in brain tissue. **Left:** Zoom view of the
335 Gd distribution. The deposits contained most of the Gd in the brain tissue sample. The
336 centre of the deposits exhibited highest concentrations exceeding 1 $\mu\text{g/g}$. **Right:** Overlay
337 of the P distribution (red) and the Gd distribution (green). Correlations are shown in
338 yellow showing a uniform distribution of P and ^{158}Gd within the deposits.

339 1.3 Conclusion

340 The newly developed method was suitable for the quantification of various
341 elements that are important for the investigation of Gd retention in patients who
342 have undergone MRI diagnostics after administration of Gd-based contrast
343 agents. Tandem mass spectrometry resulted in superior detection limits for Gd,
344 P, Fe, Zn, and Ca when compared against a standard SQ based method for EBI.
345 The improved detection tune was suitable for investigation of Gd depositions in
346 NSF skin and brain tissues at high spatial resolution ($5\mu\text{m} \times 5\mu\text{m}$). The Gd

347 distribution was quantified employing matrix matched tissue standards enabling
348 the calibration of small Gd deposits, also observed in other studies, with
349 diameters of approximately 50 μm for the first time. The analysis furthermore
350 allowed the high spatial resolution of P, Zn, Ca and Fe and enabled the
351 identification of correlations. The results support the hypothesis that Gd is
352 liberated in a transmetallation process and precipitated as an insoluble
353 phosphate salt. This method is a viable tool for analyses requiring higher
354 resolutions or lower detection limits of elements taking part in the pathogenesis
355 of NSF and the deposition of Gd in brain tissue.

356 **Acknowledgment**

357 Images were analysed and created using imaging software by Robin Schmid
358 (University of Muenster).

359 PAD is the recipient of an Australian Research Council Discovery Project
360 (DP170100036).

361 **References**

- 362 [1] T. Grobner, Gadolinium - a specific trigger for the development of
363 nephrogenic fibrosing dermopathy and nephrogenic systemic fibrosis?,
364 *Nephrol. Dial. Transplant.* 21 (2006) 1104–1108. doi:10.1093/ndt/gfk062.
- 365 [2] S.E. Cowper, H.S. Robin, S.M. Steinberg, L.D. Su, S. Gupta, P.E. LeBoit,
366 *Scleromyxoedema-like cutaneous diseases in renal-dialysis patients,*
367 *Lancet.* 356 (2000) 1000–1001. doi:10.1016/S0140-6736(00)02694-5.
- 368 [3] P. Marckmann, L. Skov, K. Rossen, A. Dupont, M.B. Damholt, J.G. Heaf,
369 H.S. Thomsen, Nephrogenic systemic fibrosis: suspected causative role
370 of gadodiamide used for contrast-enhanced magnetic resonance imaging,
371 *J. Am. Soc. Nephrol.* 17 (2006) 2359–2362.
- 372 [4] M. Birka, K.S. Wentker, E. Lusmöller, B. Arheilger, C.A. Wehe, M.
373 Sperling, R. Stadler, U. Karst, *Diagnosis of Nephrogenic Systemic*

- 374 Fibrosis by means of Elemental Bioimaging and Speciation Analysis,
375 Anal. Chem. 87 (2015) 3321–3328. doi:10.1021/ac504488k.
- 376 [5] S. Swaminathan, W.A. High, J. Ranville, T.D. Horn, K. Hiatt, M. Thomas,
377 H.H. Brown, S. V. Shah, Cardiac and vascular metal deposition with high
378 mortality in nephrogenic systemic fibrosis., *Kidney Int.* 73 (2008) 1413–
379 1418. doi:10.1038/ki.2008.76.
- 380 [6] S. Kasahara, Y. Miki, M. Kanagaki, A. Yamamoto, N. Mori, T. Sawada, T.
381 Taoka, T. Okada, K. Togashi, Hyperintense dentate nucleus on
382 unenhanced T1-weighted MR images is associated with a history of brain
383 irradiation., *Radiology.* 258 (2011) 222–228. doi:10.1148/radiol.10100508.
- 384 [7] D. Xia, R.L. Davis, J.A. Crawford, J.L. Abraham, Gadolinium released
385 from MR contrast agents is deposited in brain tumors: in situ
386 demonstration using scanning electron microscopy with energy dispersive
387 X-ray spectroscopy., *Acta Radiol.* 51 (2010) 1126–1136.
388 doi:10.3109/02841851.2010.515614.
- 389 [8] FDA Drug Safety Communication, FDA evaluating the risk of brain
390 deposits with repeated use of gadolinium-based contrast agents for
391 magnetic resonance imaging (MRI), (2015).
- 392 [9] D. Clases, M. Sperling, U. Karst, Analysis of metal-based contrast agents
393 in medicine and the environment, *TrAC - Trends Anal. Chem.* 104 (2018).
394 135-147. doi:10.1016/j.trac.2017.12.011.
- 395 [10] Y. Cao, D.Q. Huang, G. Shih, M.R. Prince, Signal change in the dentate
396 nucleus on T1-weighted MR images after multiple administrations of
397 gadopentetate dimeglumine versus gadobutrol, *Am. J. Roentgenol.* 206
398 (2016) 414–419. doi:10.2214/AJR.15.15327.
- 399 [11] N. Murata, L.F. Gonzalez-Cuyar, K. Murata, C. Fligner, R. Dills, D. Hippe,
400 K.R. Maravilla, Macrocyclic and Other Non–Group 1 Gadolinium Contrast
401 Agents Deposit Low Levels of Gadolinium in Brain and Bone Tissue,

- 402 Invest. Radiol. 51 (2016) 447–53. doi:10.1097/RLI.0000000000000252.
- 403 [12] A.P. Kartamihardja, T. Nakajima, S. Kameo, H. Koyama, Y. Tsushima,
404 Impact of Impaired Renal Function on Gadolinium Retention After
405 Administration of Gadolinium-Based Contrast Agents in a Mouse Model,
406 Invest. Radiol. 51 (2016) 655–660. doi:10.1097/RLI.0000000000000295.
- 407 [13] T.F. Flood, N. V Stence, J.A. Maloney, D.M. Mirsky, Pediatric Brain:
408 Repeated Exposure to Linear Gadolinium-based Contrast Material Is
409 Associated with Increased Signal Intensity at Unenhanced T1-weighted
410 MR Imaging., Radiology. 282 (2016) 222–228.
411 doi:10.1148/radiol.2016160356.
- 412 [14] M. Birka, J. Roscher, M. Holtkamp, M. Sperling, U. Karst, Investigating
413 the stability of gadolinium based contrast agents towards UV radiation,
414 Water Res. 91 (2016) 244–250. doi:10.1016/j.watres.2016.01.012.
- 415 [15] D.R. Roberts, S.M. Lindhorst, C.T. Welsh, K.R. Maravilla, M.N. Herring,
416 A.K. Braun, B.H. Thiers, W.C. Davis, High Levels of Gadolinium
417 Deposition in the Skin of a Patient With Normal Renal Function., Invest.
418 Radiol. 51 (2016) 280–289. doi:10.1097/RLI.0000000000000266.
- 419 [16] S. Fingerhut, A.-C. Niehoff, M. Sperling, A. Jeibmann, W. Paulus, T.
420 Niederstadt, T. Allkemper, W. Heindel, M. Holling, U. Karst, Spatially
421 resolved quantification of gadolinium deposited in the brain of a patient
422 treated with gadolinium-based contrast agents, J. Trace Elem. Med. Biol.
423 45 (2018) 125–130. doi:https://doi.org/10.1016/j.jtemb.2017.10.004.
- 424 [17] S. Fingerhut, M. Sperling, M. Holling, T. Niederstadt, T. Allkemper, A.
425 Radbruch, W. Heindel, W. Paulus, A. Jeibmann, U. Karst, Gadolinium-
426 based contrast agents induce gadolinium deposits in cerebral vessel
427 walls, while the neuropil is not affected: an autopsy study, Acta
428 Neuropathol. 136 (2018) 127–138. doi:10.1007/s00401-018-1857-4.
- 429 [18] S. Swaminathan, Gadolinium toxicity : Iron and ferroportin as central

- 430 targets, *Magn. Reson. Imaging*. 34 (2016) 1373-1376.
431 doi:10.1016/j.mri.2016.08.016.
- 432 [19] C. Thakral, J.L. Abraham, Gadolinium-induced nephrogenic systemic
433 fibrosis is associated with insoluble Gd deposits in tissues: In Vivo
434 transmetallation confirmed by microanalysis, *J. Cutan. Pathol.* 36 (2009)
435 1244–1254. doi:10.1111/j.1600-0560.2009.01283.x.
- 436 [20] S.J. George, S.M. Webb, J.L. Abraham, S.P. Cramer, Synchrotron X-ray
437 analyses demonstrate phosphate-bound gadolinium in skin in
438 nephrogenic systemic fibrosis, *Br. J. Dermatol.* 163 (2010) 1077–1081.
439 doi:10.1111/j.1365-2133.2010.09918.x.
- 440 [21] S.G. Schäd, P. Heitland, W.N. Kühn-Velten, G.E. Gross, L. Jonas, Time-
441 dependent decrement of dermal gadolinium deposits and significant
442 improvement of skin symptoms in a patient with nephrogenic systemic
443 fibrosis after temporary renal failure, *J. Cutan. Pathol.* 40 (2013) 935–944.
444 doi:10.1111/cup.12214.
- 445 [22] J.L. Abraham, S. Chandra, C. Thakral, J.M. Abraham, SIMS imaging of
446 gadolinium isotopes in tissue from Nephrogenic Systemic Fibrosis
447 patients: Release of free Gd from magnetic resonance imaging (MRI)
448 contrast agents, *Appl. Surf. Sci.* 255 (2008) 1181–1184.
449 doi:10.1016/j.apsusc.2008.05.140.
- 450 [23] R.J. McDonald, J.S. McDonald, D.F. Kallmes, M.E. Jentoft, D.L. Murray,
451 K.R. Thielen, E.E. Williamson, L.J. Eckel, Intracranial Gadolinium
452 Deposition after Contrast-enhanced MR Imaging., *Radiology*. 275 (2015)
453 772–82. doi:10.1148/radiol.15150025.
- 454 [24] J.A. Schroeder, C. Weingart, B. Coras, I. Hausser, S. Reinhold, M. Mack,
455 V. Seybold, T. Vogt, B. Banas, F. Hofstaedter, B.K. Krämer,
456 Ultrastructural evidence of dermal gadolinium deposits in a patient with
457 nephrogenic systemic fibrosis and end-stage renal disease, *Clin. J. Am.*

- 458 Soc. Nephrol. 3 (2008) 968–975. doi:10.2215/CJN.00100108.
- 459 [25] C. Thakral, J. Alhariri, J.L. Abraham, Long-term retention of gadolinium in
460 tissues from nephrogenic systemic fibrosis patient after multiple
461 gadolinium-enhanced MRI scans: Case report and implications, *Contrast*
462 *Media Mol. Imaging.* 2 (2007) 199–205. doi:10.1002/cmml.146.
- 463 [26] J.L. Abraham, C. Thakral, L. Skov, K. Rossen, P. Marckmann, Dermal
464 inorganic gadolinium concentrations: Evidence for in vivo transmetallation
465 and long-term persistence in nephrogenic systemic fibrosis, *Br. J.*
466 *Dermatol.* 158 (2008) 273–280. doi:10.1111/j.1365-2133.2007.08335.x.
- 467 [27] W.A. High, R.A. Ayers, J. Chandler, G. Zito, S.E. Cowper, Gadolinium is
468 detectable within the tissue of patients with nephrogenic systemic fibrosis,
469 *J. Am. Acad. Dermatol.* 56 (2007) 21–26. doi:10.1016/j.jaad.2006.10.047.
- 470 [28] R.C. Semelka, M. Ramalho, M. AlObaidy, J. Ramalho, Gadolinium in
471 humans: A family of disorders, *Am. J. Roentgenol.* 207 (2016) 229–233.
472 doi:10.2214/AJR.15.15842.
- 473 [29] D.P. Bishop, D. Clases, F. Fryer, E. Williams, S. Wilkins, D.J. Hare, N.
474 Cole, U. Karst, P.A. Doble, Elemental bio-imaging using laser ablation-
475 triple quadrupole-ICP-MS, *J. Anal. At. Spectrom.* 31 (2016) 197–202.
476 [http://www.scopus.com/inward/record.url?eid=2-s2.0-](http://www.scopus.com/inward/record.url?eid=2-s2.0-84952894964&partnerID=tZOtx3y1)
477 [84952894964&partnerID=tZOtx3y1.](http://www.scopus.com/inward/record.url?eid=2-s2.0-84952894964&partnerID=tZOtx3y1)
- 478 [30] L. Balcaen, E. Bolea-Fernandez, M. Resano, F. Vanhaecke, Inductively
479 coupled plasma - Tandem mass spectrometry (ICP-MS/MS): A powerful
480 and universal tool for the interference-free determination of (ultra)trace
481 elements - A tutorial review, *Anal. Chim. Acta.* 894 (2015) 7–19.
482 doi:10.1016/j.aca.2015.08.053.
- 483 [31] E. Bolea-Fernandez, L. Balcaen, M. Resano, F. Vanhaecke, Overcoming
484 spectral overlap via inductively coupled plasma-tandem mass
485 spectrometry (ICP-MS/MS). A tutorial review, *J. Anal. At. Spectrom.* 32

486 (2017) 1660–1679. doi:10.1039/C7JA00010C.

487 [32] D.J. Hare, J. Lear, D. Bishop, A. Beavis, P.A. Doble, Protocol for
488 production of matrix-matched brain tissue standards for imaging by laser
489 ablation-inductively coupled plasma-mass spectrometry, *Anal. Methods*. 5
490 (2013) 1915–1921. doi:10.1039/c3ay26248k.

491 [33] J. Lear, D.J. Hare, F. Fryer, P.A. Adlard, D.I. Finkelstein, P.A. Doble,
492 High-resolution elemental bioimaging of Ca, Mn, Fe, Co, Cu, and Zn
493 employing LA-ICP-MS and hydrogen reaction gas, *Anal. Chem.* 84 (2012)
494 6707–6714. doi:10.1021/ac301156f.

495